Velocity Structure and Variability of [O III] Emission in Black Hole Host Globular Cluster RZ2109

Matthew M. Steele[1], Stephen E. Zepf[1], Arunav Kundu[1,2], Thomas J. Maccarone[3], Katherine L. Rhode[4], and John J. Salzer[4]

ABSTRACT

We present a multi-facility study of the optical spectrum of the extragalactic globular cluster RZ2109, which hosts a bright black hole X-ray source. The optical spectrum of RZ2109 shows strong and very broad [O III]$\lambda\lambda$4959,5007 emission in addition to the stellar absorption lines typical of a globular cluster. We use observations over an extended period of time to constrain the variability of these [O III] emission lines. We find that the equivalent width of the lines is similar in all of the datasets; the change in L[O III]λ5007 is $\lesssim$ 10% between the first and last observations, which were separated by 467 days. The velocity profile of the line also shows no significant variability over this interval. Using a simple geometric model we demonstrate that the observed [O III]λ5007 line velocity structure can be described by a two component model with most of the flux contributed by a bipolar conical outflow of about 1,600 km s^{-1}, and the remainder from a Gaussian component with a FWHM of several hundred km s^{-1}.

Subject headings: galaxies: individual (NGC 4472) — galaxies: star clusters: individual (NGC 4472) — globular clusters: general — X-rays: binaries — X-rays: galaxies: clusters

1. INTRODUCTION

The first unambiguous black hole X-ray source in a globular cluster was discovered by Maccarone et al. (2007) in the extragalactic globular cluster RZ2109. This globular cluster is in the Virgo elliptical galaxy NGC 4472 (M49), and is a luminous, metal-poor cluster, with an absolute magnitude of $M_V = -10.0$ and a B-V color of 0.68, located 6.6′ away from the center of its host galaxy (Rhode & Zepf 2001). The black hole X-ray source in RZ2109 was discovered in XMM observations of the NGC 4472 globular cluster system, of which RZ2109 is a member. The

[1]Department of Physics & Astronomy, Michigan State University, East Lansing, MI 48824; e-mail: steele24@msu.edu

[2]Eureka Scientific, 2452 Delmer Street Suite 100, Oakland, CA 94602-3017

[3]School of Physics & Astronomy, University of Southampton, Southampton, Hampshire S017 1BJ, UK

[4]Department of Astronomy, Indiana University, Bloomington, IN 47405

XMM observations of the source XMMU122939.7+075333 in RZ2109 showed that it had a X-ray luminosity of $\simeq 4 \times 10^{39}$ ergs s^{-1} with x-ray counts that varied by a factor of 7 over a few hours (Maccarone et al. 2007). The high X-ray luminosity, more than an order of magnitude higher than the Eddington luminosity for a neutron star, requires either a black hole or multiple neutron stars in the old population of the globular cluster. The strong variability within the XMM observation rules out multiple neutron stars, and indicates that the source is a black-hole system (Maccarone et al. 2007).

A study of existing optical spectra of RZ2109 revealed that it had broad, strong [O III]λ5007 emission at the absorption line radial velocity of the globular cluster (Zepf et al. 2007). Follow-up optical spectroscopy with the Keck telescope showed stellar absorption lines typical of an old globular cluster and remarkably broad and luminous [O III]$\lambda\lambda$4959,5007 emission lines (Zepf et al. 2008, hereafter Z08). Specifically, Z08 showed that the velocity width of the [O III]λ5007 line is $\simeq 2,000$ km s^{-1}, and that the line luminosity is about 1.4×10^{37} ergs s^{-1}. Moreover, there is no sign of emission lines other than [O III], and the L([O III])/L(Hβ) ratio appears to be at least 30 (Z08).

The observed high luminosity and broad velocity width of the [O III]$\lambda\lambda$4959,5007 emission lines place strong constraints on the origin of these emission lines and the nature of the black hole X-ray source in RZ2109. For example, the presence of this very strong and broad [O III] emission in the black hole X-source hosting globular cluster RZ2109 and the absence of similar emission in any other spectroscopic study of globular clusters argues strongly against significant beaming of the X-rays (Gnedin et al. 2009). Furthermore, Z08 showed that the observed broad [O III]$\lambda\lambda$4959,5007 velocities cannot be explained by gravitational motions near the black hole because the available volume sufficiently close to the black hole is many orders of magnitude too small to produce the observed [O III]λ5007, given the critical density of the line. Instead, the broad velocity and high luminosity requires a strong outflow from the accreting black hole. Z08 suggests that such strong outflows occur for systems near their Eddington limit (see also Proga 2007, and references therein). The observed L_X of $\simeq 4 \times 10^{39}$ ergs s^{-1} thus indicates a stellar mass for the accreting black hole in the globular cluster RZ2109 (see discussion in Z08).

In this study we present several sets of new optical spectroscopic data on the broad [O III]$\lambda\lambda$4959,5007 lines in RZ2109. We use the multiple observations at different times to study the variability of the [O III]$\lambda\lambda$4959,5007 emission over baselines ranging from one to 467 days. We also take advantage of the higher signal-to-noise and higher spectral resolution of our new Gemini data to constrain models of the [O III]$\lambda\lambda$4959,5007 emitting regions.

2. OBSERVATIONS AND DATA REDUCTION

In this study we use medium resolution optical spectra of RZ2109 from four observatories. One set of observations has been previously presented, and the other three are described for the first time here. The four sets of observations span an interval of 467 days from the initial to the most recent observation.

2.1. Keck

Optical spectra were obtained using the Low Resolution Imaging Spectrograph (Oke et al. 1995) on the Keck Telescope. These data, originally reported in Z08, have a wavelength coverage of 3200–5500, 5800–8930 Å and a measured spectral resolution of R $\sim$ 400. The spectra were collected on the nights of UT 2007 December 17–18.

2.2. WHT

Observations were made on UT 2008 January 5–6 using the 4.2 m William Herschel Telescope (WHT) with the Intermediate dispersion Spectrograph and Imaging System operating in longslit mode. The WHT spectra have a wavelength coverage of 3900–5350, 5390–10000 Å and a measured resolution of R $\sim$ 660. To produce these observations the spectrograph was set up using the 1.53 arcsec slit with the R300B grating in the blue arm and the R158R grating in the red arm. For purposes of calibration the standard star HZ44 was observed using an identical instrumental setup.

2.3. SOAR

Observations from Goodman High Throughput Spectrograph (Clemens et al. 2004) on the 4.1m Southern Astrophysical Research Telescope (SOAR) were collected on UT 2009 January 23, 24 and February 22. The SOAR spectra have a wavelength coverage of 4352–7024 Å and a measured resolution of R $\sim$ 1600, using the KOSI 600 grating and a slit width of 0.84 arcsec.

2.4. Gemini

Spectra from the Gemini South Telescope were obtained under a queue observation using the Gemini Multi-Object Spectrograph (Hook et al. 2004) in longslit mode. The data were obtained on the nights of UT 2009 March 28, 29 and 30 (program GS-2009A-Q-1). The instrumental setup included the use of the B1200 grating with a slit width of 1.0 arcsec. This setup produced a wavelength coverage for the resulting spectra is 4445–6023 Å with a measured spectral resolution of R $\sim$ 2400.

2.5. Data Reduction

All data presented for the first time in this work were reduced using standard IRAF NOAO longslit tools, including the Gemini IRAF package for the Gemini data. The processed two dimensional spectra were extracted and, except where noted in Section 3.2, the data from the same facility obtained on consecutive nights were co-added to increase the signal-to-noise ratio of each observation. The low signal-to-noise of the SOAR observations due to the smaller instrument aperture and relative inefficiency of the spectrograph at the time necessitated co-addition of the two dimensional spectra prior to extraction of the one dimensional spectrum. The WHT spectrum was flux calibrated using observations of standard star HZ44; all other spectra were left uncalibrated and simply normalized to a polynomial continuum fit. For the [O III] line profile measurements and modeling presented in this work, simple continuum normalization is sufficient. Flux calibration is useful for analysis of the stellar component of the spectrum, where the detailed flux of the continuum contains information on the cluster's stellar population.

The stellar component of the globular cluster is fitted with a synthetic stellar spectrum as described in Section 2.6. The best fit model is used to account for and remove any effect of the overall stellar population of the globular cluster on the measurement of the emission line equivalent width in Section 3.1. The [O III] emission line complex is then analyzed for variability in Section 3 and the velocity profile is modeled in Section 4 to investigate the geometry of the emitting region.

2.6. Stellar Component Model

The observed spectra presented in this work are a superposition of the emission line system of interest and the emission from stars of the host globular cluster. In order to analyze the emission line system we first fit and subtract the stellar component. In fitting the stellar component we follow the prescription of Koleva et al. (2008). A grid of synthetic spectra was created using the Pegasè-HR code of Le Borgne et al. (2004) and the Elodie 3.1 spectral library (Prugniel et al. 2007). The models assumed a Salpeter initial mass function (IMF) and a single epoch of star formation in the cluster. The synthetic spectra were fit using the WHT data due to its large wavelength coverage and moderate instrumental resolution. The WHT data were masked to exclude the region of [O III]$\lambda\lambda4959, 5007$ and Hβ to eliminate any effects of emission lines. The data were then fitted using the grid of spectra which yielded a best fit model with an age of 12 Gyr and an initial [Fe/H] of -1.2. In order to test this model fitting scheme an independent set of synthetic stellar population models from Vazdekis et al. (2007) were re-sampled and injected with noise to match our data, and then fit using the method described above. This test yielded estimates of the uncertainty in the stellar component parameters contributed by the model fitting scheme of ±1.5 Gyr in age and ±0.05 dex in metallicity. Given the uncertainties in the stellar population models and the assumptions used in the generation of the synthetic spectra, we adopt total uncertainties of age ±2 Gyr and metallicity ±0.1 dex. Repeating the stellar component fitting while adopting an

IMF for Kroupa (2001) produces fit stellar parameters of 14 Gyr and [Fe/H] of -1.1. Both these parameters are within the estimated uncertainties of the modeling and fitting procedure, suggesting the effect of IMF selection on the resulting stellar component model is minimal for this study. In Maccarone et al. (2007) a value of [Fe/H]=-1.7 ± 0.2 and an old stellar population age was inferred from the optical colors of Rhode & Zepf (2001). These parameters are in reasonable agreement with the values we find here. A more detailed analysis of the stellar component of the globular cluster will be presented in a forthcoming work (Steele et al. 2011, in prep).

The stellar population parameters determined above were used to construct synthetic spectra to match the wavelength coverage and spectral resolution of each observation. These synthetic spectra were then used to remove the stellar component from each observation.

3. VARIABILITY

A careful study of the variability of the [O III] complex equivalent width and velocity structure, when combined with the x-ray variability timescales, potentially provides information on the size and density structure of the emitting region. By examining the equivalent width of the [O III] over various timescales it is possible to constrain the ionizing photon path length and estimate the size of the emitting region. The emission line velocity structure, coupled with any variability in X-ray data, may also help constrain other physical properties of the emitting material.

3.1. Equivalent Width Variability

Line equivalent widths were measured by direct integration under the line profile and bounded by a linear fit to the local continuum. The [O III]$\lambda\lambda$4959,5007 emission is observed as a blended feature, due to the very broad width of each [O III] line, as seen in Figure 1. The [O III]$\lambda\lambda$4959,5007 emission lines and the stellar absorption of the globular cluster RZ2109 are also found to have a redshift of 1475 km s^{-1} (Zepf et al. 2007). Therefore, the equivalent width of the entire complex was measured between the observed wavelengths of 4964 Å and 5058 Å, which are symmetric in velocity space about the midpoint of the redshifted broad [O III]$\lambda\lambda$4959,5007 emission and beyond which the emission flux is indistinguishable from zero. The equivalent widths of the individual λ5007 and λ4959 lines were then set by the ratio established by their respective transition probabilities. Identical measurements were performed on the stellar component models and the resulting values subtracted from the data measurements to yield equivalent widths of the emission component. Uncertainty estimates for the equivalent widths were generated by considering a systematic contribution (instrumental noise, poor cosmic ray subtraction, etc.) and a photon statistic contribution. The systematic contribution was estimated by measuring the per pixel root-mean-squared (RMS) deviation from the continuum of two regions located to the red and blue side of the emission feature which were free of strong stellar absorption features. The two uncertainty contributions were added by quadrature to produce the given values.

Table 1 displays the measured equivalent widths of the [O III]λ5007 for each observation along with the date of observation. The uncertainty-weighted mean of all observation is 33.4 ± 0.3 Å with little change observed over the course of our observations. For the longest time baseline between the first observation with the Keck telescope to the last with Gemini-South, we find very close agreement in the [O III]λ5007 emission, with a a difference of only $\sim 9 \pm 2\%$ between these observations separated by 467 days. The intervening WHT and SOAR data have larger uncertainties, but no observation deviates strongly from the mean [O III] equivalent width, with the WHT observation being the most offset with a formal difference of $27.5 \pm 7.5\%$ from the weighted mean.

3.2. Line Profile Variability

It is possible to examine the internight variability of the [O III] complex velocity profile using the Gemini spectra co-added for each of the three consecutive nights of observation. In Figure 2 the three two hour exposures are displayed. A visual inspection of the three spectra does not reveal any obvious variability over the region displayed. To test the line profile variability each spectrum was divided into 5 Å bins and subtracted from the other two binned spectra. The differences in the bins in the [O III] region were then calculated in terms of the RMS of the differences in bins not containing [O III] emission. Of the 57 comparison bins in the [O III] region, 17 displayed differences larger than 1σ, two larger than 2σ and none larger than 3σ. For these differences, seven of the 17 1σ deviations were above the continuum and ten were below it. These numbers are consistent with the RMS statistical expectations, indicating no evidence for variability in the velocity structure over the three nights observed.

A similar approach may be used to probe a longer temporal scale by a comparison of the Keck and Gemini spectra. For this analysis the six hours of Gemini integrations are co-added and convolved with the Keck instrumental resolution. The Keck and convolved Gemini spectra are displayed in Figure 3. A visual inspection reveals that when the resolution of the two spectra are matched, the observations are consistent. A similar analysis as performed on the Gemini individual night spectra yields 11 bins in the [O III] emitting region, four of which have differences greater than 1σ, one greater 2σ and none the greater than 3σ. These results are again consistent with the RMS statistical expectations. The 10 Å bin with the greatest difference of 2.4 σ is centered at 5063 Å , on the extreme red side of the emission complex. By eye it is possible to pick out a small excess of emission in what appears to be a 'secondary peak' on the blue side of both the [O III]λ4959 and [O III]λ5007 structures in the Keck spectrum. However when the λ4959 and λ5007 lines are transformed to velocity space these 'secondary peaks' are separated by 330 km s^{-1}, suggesting they are not real structures.

4. GEOMETRIC MODEL

An initial qualitative inspection of the [O III]$\lambda\lambda 4959, 5007$ velocity structure line profile reveals that the complex may be divided into a λ4959 line and a λ5007 line shown in Figure 4. Theoretical considerations dictate that these two lines should display identical line profile shapes and differ only in their total flux level, the ratio of which is set by their transition probabilities. The data are in good agreement with this expectation. The two main features of the [O III] line profiles are strong broad emission spanning between ∼300–1300 km s^{-1}, and a central, narrower peak. At larger velocities the emission falls off rapidly between ∼1300–1700 km s^{-1}. While the velocity structure appears symmetric about line center, there appears to be a flux level asymmetry between the blue and red sides of the line profile.

In an effort to quantify the observed emission line profile, we fit a simple geometric model to the [O III]λ5007 line profile of the continuum normalized Gemini data. The model consists of two components; a bipolar conical outflow and a lower velocity width Gaussian component. The bipolar conical outflow produces the broad emission component, with the lower velocity width peak contributed by the Gaussian. This two component model is necessary as no model with only a bipolar conical component or only a Gaussian component was able to simultaneously reproduce flat broad component, and the narrower peak. Fitting the simple geometric model to the observations allows us to describe the emission line structure in terms of the model parameters: the velocity of the outflowing gas, the opening angle of the cones, the angle of inclination of the cone's axis relative to the observer, and the full width half maximum (FWHM) of the Gaussian component.

The resulting best fit model is displayed along with the Gemini data in Figure 5. This model has an outflow velocity of 1600^{+190}_{-90} km s^{-1}, an opening angle of 70 ± 8 degrees, and an inclination angle of 65^{+3}_{-6} degrees relative to the line of sight. The uncertainty values on these parameters indicate the value at which a given parameter produces a 3 σ deviation of the model velocity profile from the Gemini data, with the other two parameters fixed to the best fit values. It is important to note that the model parameters are not completely independent, and so these uncertainties do not demarcate a region of "acceptable" fits in parameter space. For reference we include a set of cross-sectional uncertainty contours about the best fit model parameters in figure 6. The Gaussian component of the model has a FWHM of $\sim$ 310 km s^{-1}. In this model 81 percent of the flux is contributed by the bipolar conical outflow, and the remaining 19 percent by the lower velocity width Gaussian structure. The flux ratio of the receding outflow to the approaching outflow is 1.4. This simple model provides an excellent fit to the [O III]λ5007 line profile out to ∼1300 km s^{-1} from line center. Above this velocity the data show excess emission relative to the model both at the red and blue extremes.

The model assumes an optically thin emitting region, as appropriate for [O III], and a uniform emission density. The uniform emission density is adopted to simplify the calculation, but provided there is no strong density dependence with the angular separation from the central axis, any radial dependence of the emission density will not change the velocity structure of the model line. The bulk flow velocity is taken to be constant over the outflow. This assumption, while assuredly an oversimplification, provides a reasonable description of the available data. It is worth noting that in this formulation of the geometric model, the Gaussian component does not have an explicit physical analog. A number of physical structures could produce a Gaussian velocity profile and we will consider a few possibilities in later sections.

Given the simplicity of the high velocity width bipolar conical outflow plus lower velocity width Gaussian model, we do not place great emphasis on the detailed parameters of the model fit. Broadly, the large velocity width requires a significant outflow velocity. The flux level asymmetry of red and blue high velocity structures requires a non-uniform outflow. A flat velocity profile, as observed in the high velocity width component, may also be produced by a uniform spherical outflow or approximated by a radially directed disk wind. However, the flux asymmetry of approaching and receding outflows observed favors the spatially discrete structures of the bipolar conical outflow considered above. Due to this asymmetry, the best fit profile of a spherical outflow deviates from the Gemini data at the 9 sigma level. A spherical shell will produce an identical profile to a filled sphere because, as noted above, the velocity profile of any outflow whose velocity is independent of radius, is also independent of the radial density profile. The large opening angle indicates that the outflow that fits best in this model is not from a narrowly collimated jet, but rather a broader outflow. Any model which includes the detailed hydrodynamics of the outflowing gas may deviate from the parameters generated by the purely geometric fit considered here. As such we present the model parameters as descriptive and useful for consideration of the general properties of the emitting region.

5. DISCUSSION

5.1. Variability

There are two major modes by which the observed lack of strong variability in the [O III] emission might be produced in an accreting black hole system; a steady accretion mode, or an emitting system in which the crossing time for ionizing photons is large in comparison with the variability timescale of the ionizing source. In the case of a variable ionizing source the emission variability may also contain information on the density distribution of the emitting gas. The x-ray data described in Shih et al. (2008) span nine years and display a consistent count rate between observations. The four observations described in the present work also display consistent [O III]λ5007 equivalent widths between observations. For reference the light crossing path bounded by the optical observations presented here is 0.4 pc. Both observations are consistent with a long lived steady accretion rate. The sparse temporal sampling of the data, however, does not allow tight constraints on shorter term fluctuations in either the X-ray or [O III] emission. Future x-ray observations of the RZ2109 x-ray source, XMMU 1229397+07533, with finer temporal resolution could be combined with the [O III] variability limits presented here to construct limits on the spatial scale of the emitting region. Likewise variability in the [O III] emission under constant x-ray flux could yield information on the outflow rate and density distribution.

The absence of strong variability does allow for the elimination of one class of models as the source of the observed [O III] emission. Novae shells in the local Milky War are a known source of [O III]λ5007 emission (Downes et al. 2001). The very brightest shell nova reach L([O III]λ5007) $\sim 10^{37}$ ergs and have velocity widths on the order of those observed in RZ2109 (Downes et al. 2001; Iijima & Naito 2011, for example). In contrast to the observations presented here, however, the [O III] luminosity of these sources decay by several orders of magnitude and velocity profile vary on timescales of days to weeks.

5.2. Structure of Emission Region

It is somewhat remarkable that the geometric model presented in Section 4 fits the [O III] line profile as well at it does with simplistic assumptions. There are, of course, a number of questions either not addressed or raised by the model, including the spatial scale of the emitting system, the observed flux asymmetry of the red and blue high velocity width component, the failure of the model at the extreme high velocity wings, and the nature of the low velocity Gaussian component.

The geometric model as presented is free of any spatial scaling. We must look to other means in order to place limits on the size of the outflow region. A firm lower limit may be set using the total emission from the high velocity width outflow component of the [O III]λ5007 emission, adopting a pure [O III] gas at critical density for [O III]λ5007 at a temperature of 10^4 K (Osterbrock 1989), and employing the geometry parameters found. With this minimal constraint the observed emission could originate from a region with a minimum radius of a few $\times 10^{-3}$ pc. The data do not provide a clear upper limit on the size of the emitting region, and there is no reason given the available data that the size of the [O III]λ50007 region could not be as large as the $\sim$ 10 pc extent of the globular cluster itself.

Asymmetries in the bipolar outflows are a well known feature of accreting black hole systems. When a flux asymmetry is attributed to a differential obscuration the usual pattern observed is a decrement in the flux of the receding flow produced by the additional obscuring material along the greater line of sight distance (van Groningen 1987; Peterson et al. 2000). However, we observe the opposite effect in the RZ2109, with the receding [O III] emission line 40 percent more luminous than the approaching flow. If differential obscuration contributes to the observed flux asymmetry, the obscuring media must be local to the cluster system, such as dust-bearing gas at large radius resulting from an earlier outflow of the system or interaction with a asymmetric ISM. The mechanism by which such a local obscuring media may be produced is unclear.

A second known source of flux asymmetry in outflows is Doppler boosting (Mirabel & Rodríguez 1999; Fender 2006). In Doppler boosting, however, the flux of the approaching outflow is amplified relative to the receding outflow, again opposite of the asymmetry observed in RZ2109. The different line of sight travel times of outflows toward and away from the observer can also produce asymmetric fluxes if coupled with a variable ionizing source. However, the flux asymmetry is the same in both our Keck and Gemini observations separated by more than a year, which would be very difficult to understand in such a scenario. It therefore seems most likely that the somewhat greater flux on the red side of the [O III]λ4959,λ5007 line profile relative to the blue side is a result of an intrinsic asymmetry in the source's emission density. Such an asymmetry may be attributable to either a difference in the mass of each outflow or the ionizing flux incident on them.

An expanding gas distribution such as nova shell or other remnant produced by late stage stellar evolution and ionized by an external source may produce a flux asymmetry across the velocity profile provided the gas is optically thick. Such an arrangement would allow for a flux excess of the receding side of the velocity profile relative to the approaching if the media was positioned between the observer and the ionizing source. For example, a late stage nova shell modeled with a uniform density shell illuminated by an external x-ray source produces an asymmetric velocity profile with a continuous blue to red flux gradient whose slope is set by the position of the external x-ray source. However, this type of flux asymmetry fails to provide an adequate description of flat topped step function profile observed in the [O III]λ4959,λ5007 line profiles high velocity width component.

The failure of the model at the most extreme velocities, seen in velocities in excess of $\pm$1400 km s^{-1} in Figure 5 is most likely attributable to the simplifying assumption of constant bulk velocity in the geometric model. If this is the case and the emission in these extreme velocity wings is produced by the outflow closest to the source, prior to any deceleration, with more sophisticated modeling techniques the extreme velocity wings may provide another constraint on the spatial scale of the system.

While a model with a strong bipolar outflow can naturally account for broad [O III]λ4959,λ5007 emission, the origin of the narrower Gaussian component is less clear. The observed FWHM of this lower velocity width Gaussian peak is three times the FWHM of the spectral resolution of the Gemini spectrum. Thus, the observed strongly peaked [O III]λ5007 line profile is representative of its intrinsic shape. One implication of the strongly peaked line profile is that rotation is ruled out for the origin of the observed width of the line. It is worth noting that forbidden lines such as [O III] are optically thin, and the observed profile reflects the intrinsic one, unlike the much more complex case of optically thick permitted lines such as Balmer emission lines in AGN. Therefore, for optically thin [O III], rotation naturally produces a double-peaked or flat-topped velocity profile (e.g. Clark et al. 1979), and fails badly to match the centrally peaked profile seen in the [O III] emission. For example, the specific case of a rotating Keplerian disk with an inverse square law emission density profile has a velocity profile which deviates from the observed lower velocity width [O III] component at the 7σ level in a one spectral resolution element bin about line center. In fact, instead of showing a double-horned profile or very flat-topped profile typical of rotation, the observed profile is more centrally peaked than a Gaussian at about the 3σ level. Therefore, rotation is ruled out as the source of the velocity width of the lower velocity width Gaussian component, contrary to the assumption of some modeling (Porter 2010).

The luminosity of the L([O III])λ5007 at a given velocity can also be used to determine whether the velocity width of the line can be due to gravitational motions or not. Specifically, because [O III]λ5007 is a forbidden line with a known critical density (Osterbrock 1989), we can determine the maximum possible L([O III])λ5007 within a given volume by adopting a pure [O III] gas of uniform density at its critical density. We can also compute the largest volume available sufficiently close to the black hole to account for the observed velocity width due to gravitational motions about the black hole. Zepf et al. (2008) carried out this calculation for the broad velocity component of the [O III]λ5007, and showed it is many orders of magnitude stronger than can be accounted for with gravitational motions, and to thus require strongly outflowing material.

Here we apply this same calculation to the lower velocity width Gaussian component which is seen much more clearly in our new Gemini data with its greater spectral resolution and higher signal-to-noise. Adopting a pure [O III] gas of uniform density at its critical density (Osterbrock 1989) and a canonical black hole mass of $10\,M_{\odot}$, we find the maximum luminosity in a one resolution element bin -170 km s^{-1} from line center is of order 10^{29} ergs s^{-1}. In contrast, the observed luminosity at this velocity is 4.2×10^{35} ergs s^{-1}, and thus gravitational motions also fail to account for the velocity width of the lower velocity width Gaussian peak.

It is worth noting that the above arguments do not strictly rule out rotation of the emission line region, they do, however, require that the observed line widths be produced by some mechanism other than rotation. A scenario where the emitting region rotates in the plane of the sky, or with specific arrangements of absorbing systems may be invoked, but in these cases the line width and profile would be independent of any rotation. Because the emitting region is taken to be optically thin to the forbidden line emission observed, self absorption or intermediate line absorption systems are unlikely. Gray body or broad band absorption/scattering via an obscuring media is possible, however the specific distribution of the material necessary to transform a rotational line profile to that observed (a preferential and symmetric obscuration of the emitting gas moving parallel/anti-parallel with the line of sight) is difficult at best.

Although the specific calculation above is for a rotating sphere for simplicity, adopting a dynamically hot model for the emitting material will change the gravitational motions prediction far less than the five or more orders of magnitude difference between it and the data. The calculation also adopts a stellar mass for the black hole in the globular cluster, based on results in Z08. In that work, Z08 used the same type of volume calculation as above for the broad component of the [O III]λ5007 emission, and showed that it is not due to gravitational motions unless the black hole is nearly as massive as the $\sim 10^{6}\,M_{\odot}$ cluster itself (for a more detailed treatment see also Porter 2010). The broad component then must be due to a strong outflow. Z08 suggest that observational evidence and theoretical calculations (Proga 2007, and references therein) indicate that strong outflows are associated with high (L/$L_{\rm Edd}$) systems, which given the observed L_X, implies a stellar mass for the black hole in RZ2109.

An alternative idea, that the source could be a tidal disruption or detonation of a white dwarf by an intermediate-mass black hole, fails on several grounds (e.g. Irwin et al. 2010). A disruption is unable to account for either the high L([O III]λ5007) over an extended period of time or the long duration of its high X-ray flux from at least the early 1990s ROSAT era through 2004 (Maccarone et al. 2007; Shih et al. 2008). A detonation may account for the high velocity outflow, but does not provide an explanation for why only oxygen lines are seen in the spectrum when the detonation is powered by the fusion of oxygen into iron. Furthermore, neither a disruption or detonation is able to account for the more than a decade of consistently high L_X followed by the recently observed steep decline of L_X by more than an order of magnitude (Maccarone et al. 2010).

With the current observations we have limited ability to address the energetics of the outflow. Since we have no direct measurement of the temperature, we can estimate the mass of [O III] in the emitting region finding using a temperature typical of [O III] emission line. With an assumption of T = 10^4 K we find an [O III] mass of 7.3×10^{-5} $M_\odot$. For temperatures from 5×10^3–10^6 K the mass ranges from 1×10^{-3} to 4×10^{-6} $M_\odot$. Unfortunately since we have little to constrain either the composition of gas, beyond that it is likely hydrogen depleted, or the ionization fraction as no [O II] lines are observed above the detection threshold, we are unable to provide a concrete estimate of the total gas mass of the emitting region. For a pure oxygen gas the total mass will be within a factor of a few greater than the [O III] mass, while a solar composition would imply a total mass roughly two orders of magnitude greater. Using the 1600 km s^{-1}velocity of the higher velocity component found in Section 4 the kinetic energy of the [O III] is then 10^{45} erg. This energy is 8 orders of magnitude smaller than the available total accretion energy, assuming an accretion efficiency of 10 percent and a 1 $M_\odot$ donor. If a solar composition is assumed for the outflowing gas and all oxygen being doubly ionized the systems kinetic energy is 6 orders of magnitude smaller than the total accretion energy. It should be noted that the kinetic energy given here is for the total observed outflow; it is unknown what fraction of the total accretion event which the current outflow represents.

6. SUMMARY

In this work we have presented a study of the equivalent width and velocity profile of the [O III]$\lambda\lambda$4959, 5007 emission line complex associated with the black hole X-ray source in the extra-galactic globular cluster RZ2109. We have found little variation in the [O III]λ5007 emission in our multiple observations over a time span of 467 days. The first and last observations have a formal difference of $9 \pm 2\%$ with no evidence for different velocities, and our upper limit in the variation among all our observations is 27%. The [O III]λ5007 emission line is comprised of two components; a lower velocity width component which is well characterized by a Gaussian with FWHM 310 km s^{-1}, and high velocity width component with a width of 3200 km s^{-1} which we describe using a simple bipolar conical outflow model. The velocity width of the Gaussian component cannot be due to rotation, and both components appear to require non-gravitational motions in order to provide sufficient volume to produce the observed high luminosities in the [O III]λ5007 line.

MMS and SEZ wish to acknowledge support from NSF grants AST-0406891 and AST-0807557. AK thanks NASA for support under Chandra grant GO0-11111A. KLR acknowledges support from NSF Faculty Early Career Development grant AST-0847109. We thank the anonymous referee for the questions and critique which helped to strengthen the paper. We also thank Jack Baldwin for helpful discussion.

REFERENCES

Casares, J., Steeghs, D., Hynes, R. I., Charles, P. A., & O'Brien, K. 2003, ApJ, 590, 1041

Clark, F. O., Martin, H. M., & Biretta, J. A. 1979, ApJ, 232, 624

Clemens, J. C., Crain, J. A., & Anderson, R. 2004, Proc. SPIE, 5492, 331

Cooke, R., Bland-Hawthorn, J., Sharp, R., & Kuncic, Z. 2008, ApJ, 687, L29

Downes, R. A., Duerbeck, H. W., & Delahodde, C. E. 2001, Journal of Astronomical Data, 7, 6

Eggleton, P. P. 1983, ApJ, 268, 368

Fender, R. 2006, Compact stellar X-ray sources, 381

Gnedin, O. Y., Maccarone, T. J., Psaltis, D., & Zepf, S. E. 2009, ApJ, 705, L168

Hook, I. M., Jørgensen, I., Allington-Smith, J. R., Davies, R. L., Metcalfe, N., Murowinski, R. G., & Crampton, D. 2004, PASP, 116, 425

Iijima, T., & Naito, H. 2011, A&A, 526, A73

Irwin, J. A., Brink, T. G., Bregman, J. N., & Roberts, T. P. 2010, ApJ, 712, L1

Ivanova, N., Chaichenets, S., Fregeau, J., Heinke, C.O., Lombardi, J.C., & Woods, T.E. 2010, ApJ, 717, 948

Kaaret, P., & Corbel, S. 2009, ApJ, 697, 950

Koleva, M., Prugniel, P., Ocvirk, P., Le Borgne, D., & Soubiran, C. 2008, MNRAS, 385, 1998

Kroupa, P. 2001, MNRAS, 322, 231

Le Borgne, D., Rocca-Volmerange, B., Prugniel, P., Lançon, A., Fioc, M., & Soubiran, C. 2004, A&A, 425, 881

Macri, L. M., et al. 1999, ApJ, 521, 155

Maccarone, T. J., Kundu, A., Zepf, S. E., & Rhode, K. L. 2007, Nature, 445, 183

Maccarone, T. J., Kundu, A., Zepf, S. E., & Rhode, K. L. 2010, MNRAS, 409, L84

Mirabel, I. F., & Rodríguez, L. F. 1999, ARA&A, 37, 409

Nelemans, G., Jonker, P. G., & Steeghs, D. 2006, MNRAS, 370, 255

Oke, J. B., et al. 1995, PASP, 107, 375

Osterbrock, D. E. 1989, Astrophysics of Gaseous Nebulae and Active Galactic Nuclei (Mill Valley, CA: Univ. Science Books)

Peterson, B. M., et al. 2000, ApJ, 542, 161

Porter, R.L. 2010, MNRAS, in press

Proga, D. 2007, The Central Engine of Active Galactic Nuclei, 373, 267

Prugniel, P., Soubiran, C., Koleva, M., & Le Borgne, D. 2007, arXiv:astro-ph/0703658

Rhode, K. L., & Zepf, S. E. 2001, AJ, 121, 210

Russell, D. M., Fender, R. P., Gallo, E., & Kaiser, C. R. 2007, MNRAS, 376, 1341

Shih, I. C., Maccarone, T. J., Kundu, A., & Zepf, S. E. 2008, MNRAS, 386, 2075

Remillard, R. A., & McClintock, J. E. 2006, ARA&A, 44, 49

van Groningen, E. 1987, A&A, 186, 103

Vazdekis, A., et al. 2007, IAU Symposium, 241, 133

Werner, K., Nagel, T., Rauch, T., Hammer, N. J., & Dreizler, S. 2006, A&A, 450, 725

Zepf, S. E., Maccarone, T. J., Bergond, G., Kundu, A., Rhode, K. L., & Salzer, J. J. 2007, ApJ, 669, L69

Zepf, S. E., et al. 2008, ApJ, 683, L139

This preprint was prepared with the AAS LaTeX macros v5.2.

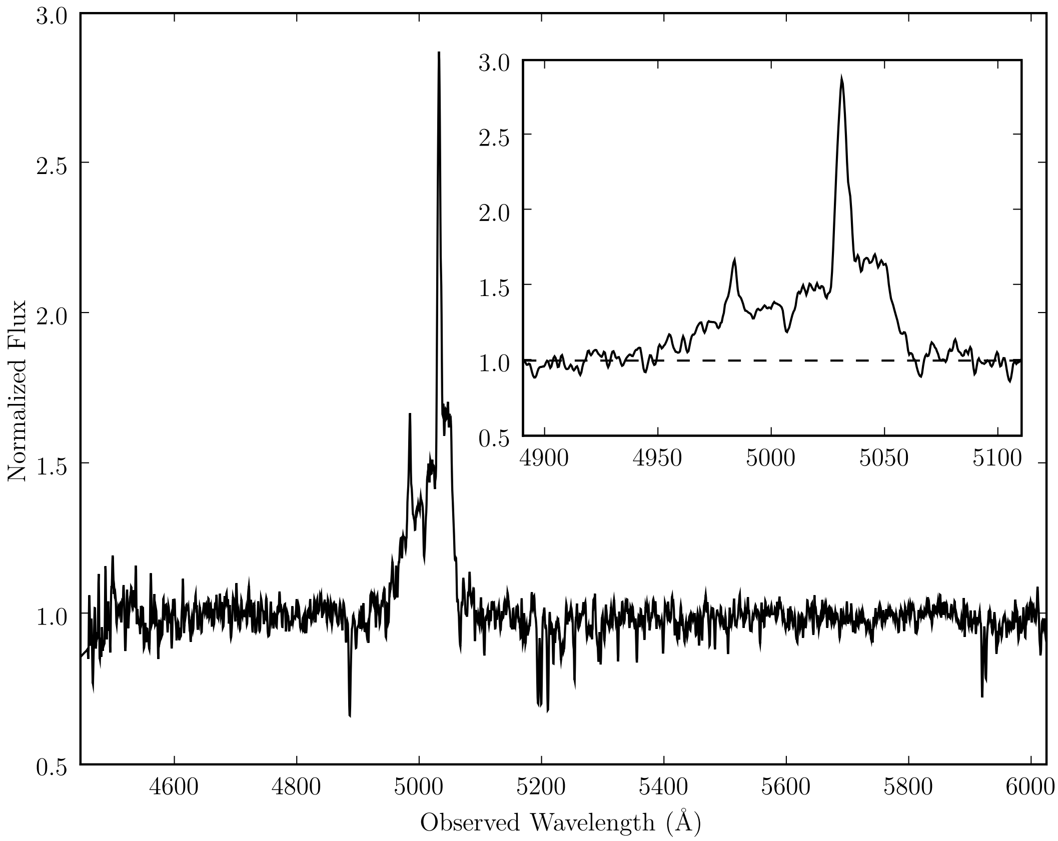

Fig. 1.— Gemini GMOS spectrum of black hole hosting globular cluster RZ2109. The inset displays the [O III]$\lambda\lambda$4959,5007 emission structure which dominates the spectrum. The spectrum has been continuum fit and normalized, and smoothed with a three pixel boxcar function.

Table 1. [O III]λ5007 Equivalent Widths

Observation	eW (Å)	Date (days)
Keck	30.9 ± 0.7	0.0
WHT	42.6 ± 2.5	20.0
SOAR	26.8 ± 8.0	434.1
GMOS	34.0 ± 0.4	467.0

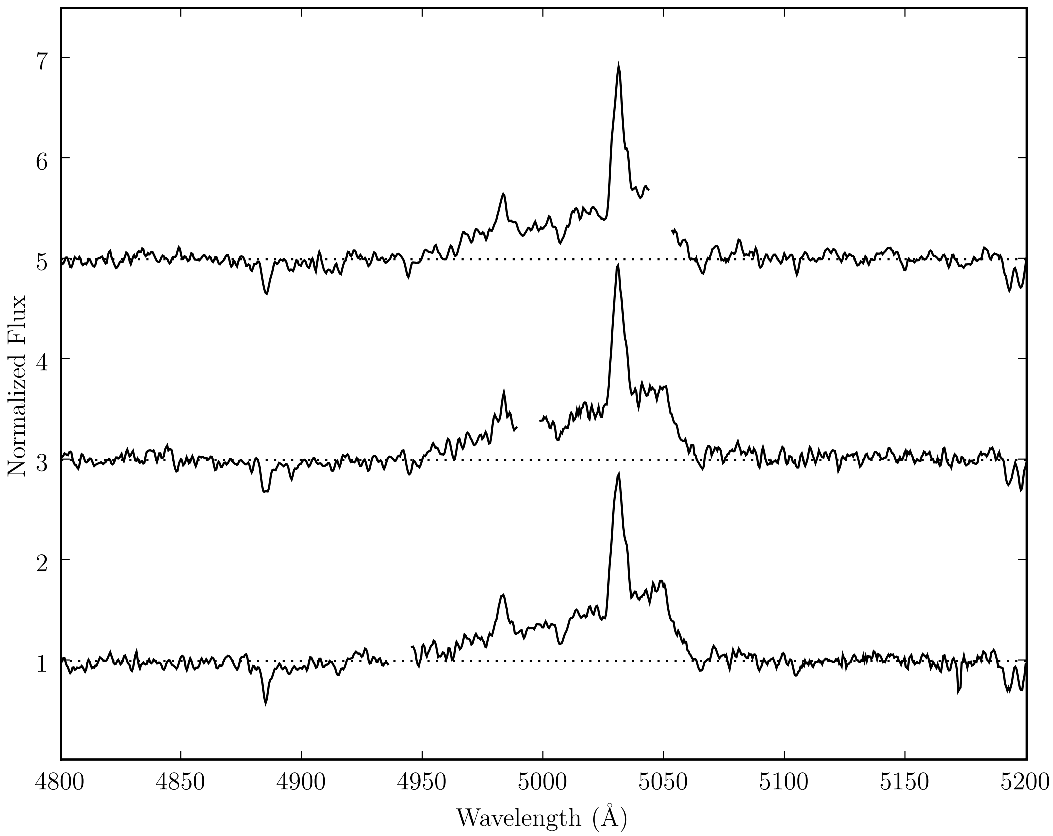

Fig. 2.— Gemini spectra internight variability. The lower (March 28, 2009), middle (March 29, 2009), and upper (March 30, 2009) spectra have been smoothed with a three pixel boxcar function and offset on the flux axis for legibility. The dashed lines give the level of the normalized continuum for reference.

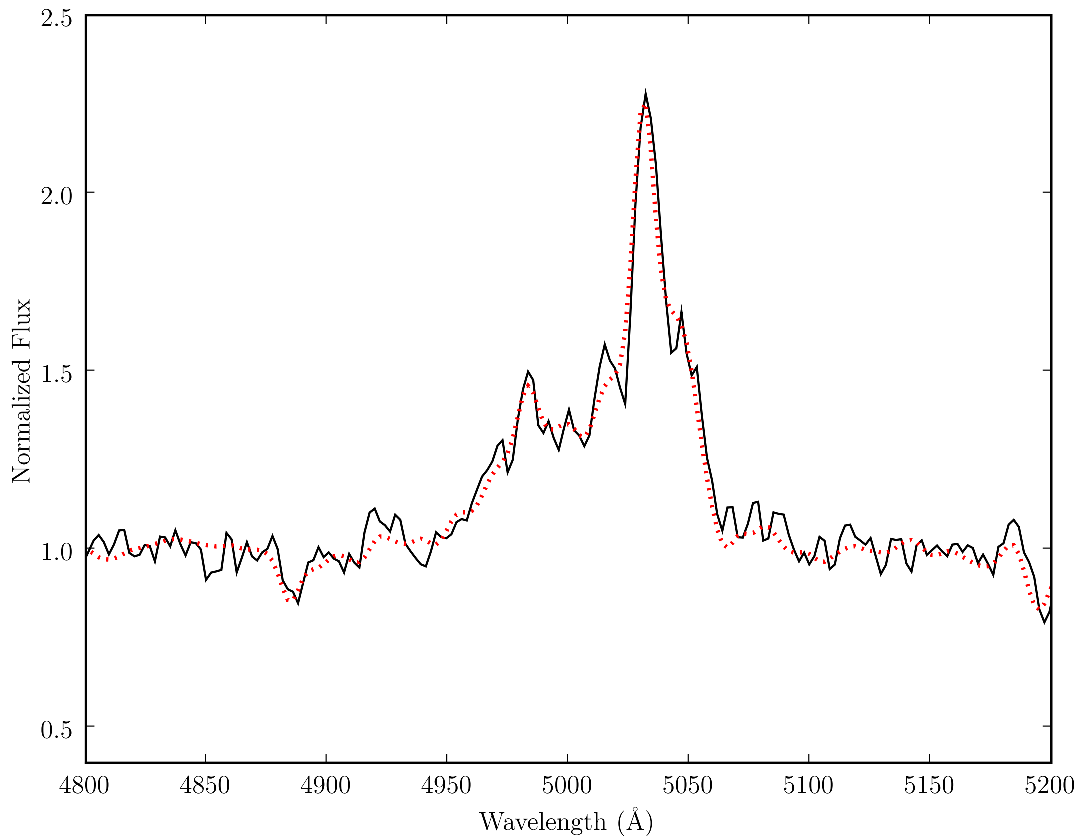

Fig. 3.— Keck and Gemini spectra comparison. The Gemini spectra (dotted line) have been convolved with the instrumental resolution of the Keck spectra (solid line.) The Keck observation preceded the Gemini observation by 467 days.

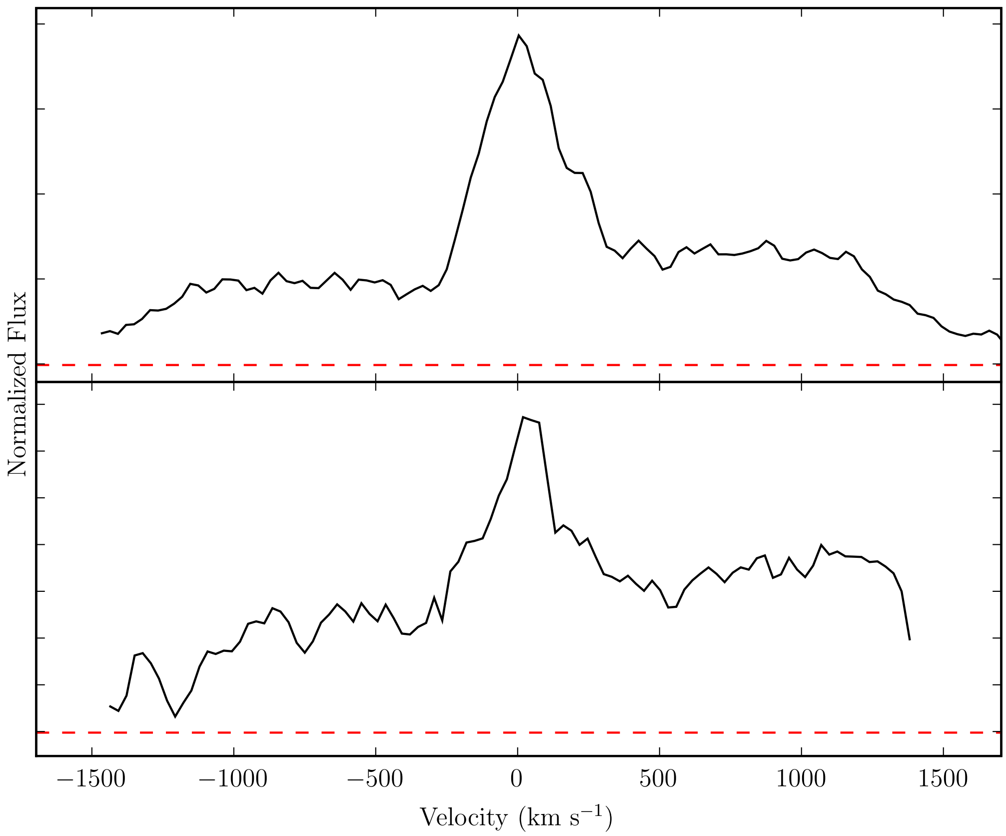

Fig. 4.— Gemini spectra [O III] velocity structure. The top figure displays the line profile for [O III]λ5007, and the lower panel [O III]λ4959. The two lines have been separated by a cut at an observed wavelength of λ5006. As a result there may be a small degree of blending on the extreme blue side of the [O III]λ5007 and the extreme red side of [O III]λ4959. The dashed lines give the continuum level for reference.

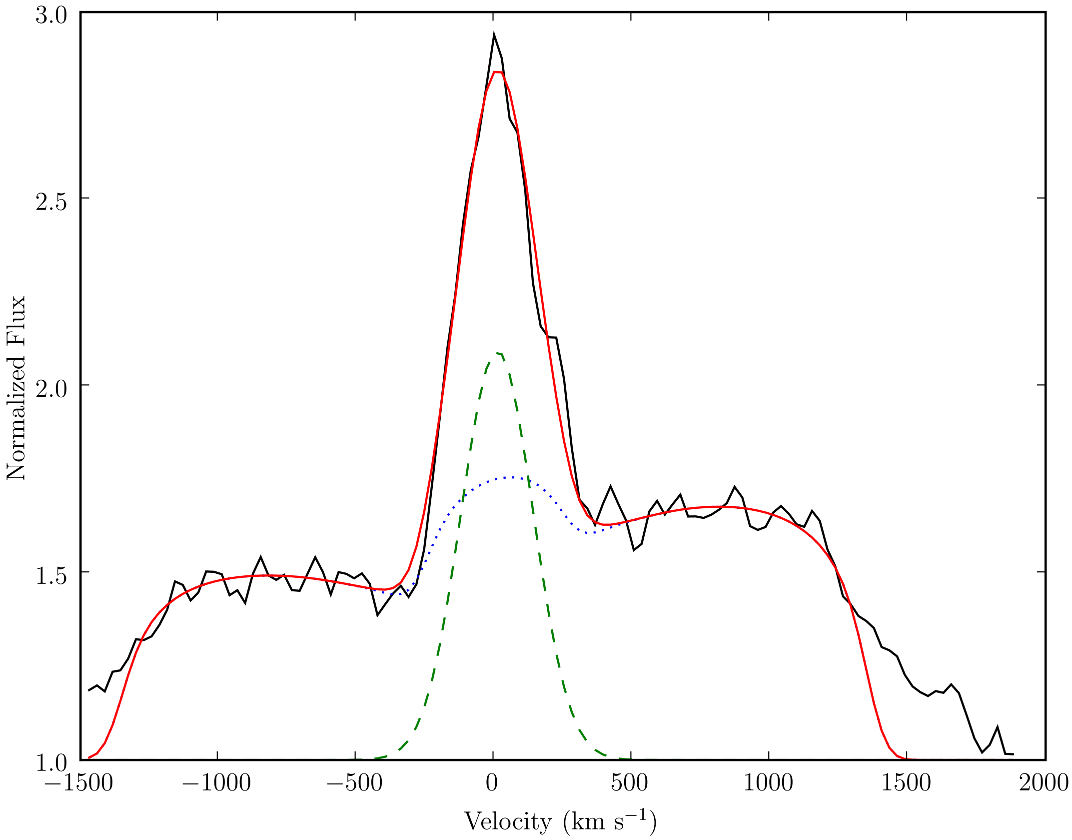

Fig. 5.— Gemini spectra with geometric model. The solid black line shows the Gemini spectra, the dotted line displays the best fit bipolar conical outflow component of the geometric model, the dashed line the Gaussian component of the model, and the solid gray line (red in the electronic version) the full geometric model.

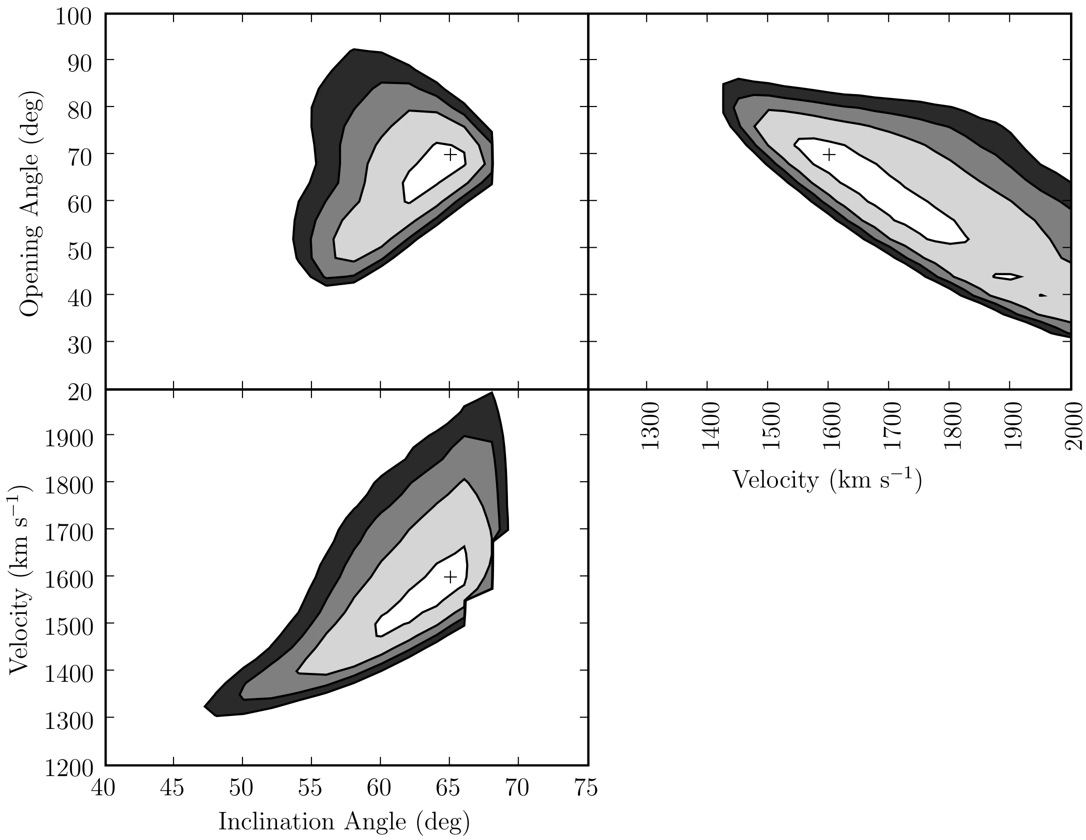

Fig. 6.— Geometric model uncertainty contours. The top left plot displays the uncertainty contours in opening and inclination angles with a fixed velocity of 1600 km s^{-1}. The top right plot give the uncertainty contours in opening angle and velocity about a fixed inclination of 65 deg. The bottom plot shows the uncertainty contours in velocity and inclination angle about a fixed opening angle of 70 deg. Contours in each plot give the 2, 3, 4, and 5 sigma deviations from the Gemini data. The plotted cross shows the position of the best fit value.